Article

The Improvement in Hydrogen Storage Performance of MgH$_2$ Enabled by Multilayer Ti$_3$C$_2$

Zhaojie Wu [1], Jianhua Fang [1,*], Na Liu [1,*], Jiang Wu [1] and Linglan Kong [2]

[1] Department of Petroleum, Oil and Lubricants, Army Logistic Academy of PLA, Chongqing 401331, China; georgewu2019@163.com (Z.W.); wujiang179@163.com (J.W.)

[2] Department of Basic Courses, Army Logistic Academy of PLA, Chongqing 401331, China; kllvj1604@163.com

* Correspondence: fangjianhua71225@sina.com (J.F.); liuna8911@163.com (N.L.)

Abstract: MgH$_2$ has become a hot spot in the research of hydrogen storage materials, due to its high theoretical hydrogen storage capacity. However, the poor kinetics and thermodynamic properties of hydrogen absorption and desorption seriously hinder the development of this material. Ti-based materials can lead to good effects in terms of reducing the temperature of MgH$_2$ in hydrogen absorption and desorption. MXene is a novel two-dimensional transition metal carbide or carbonitride similar in structure to graphene. Ti$_3$C$_2$ is one of the earliest and most widely used MXenes. Single-layer Ti$_3$C$_2$ can only exist in solution; in comparison, multilayer Ti$_3$C$_2$ (ML-Ti$_3$C$_2$) also exists as a solid powder. Thus, ML-Ti$_3$C$_2$ can be easily composited with MgH$_2$. The MgH$_2$+ML-Ti$_3$C$_2$ composite hydrogen storage system was successfully synthesized by ball milling. The experimental results show that the initial desorption temperature of MgH$_2$-6 wt.% ML-Ti$_3$C$_2$ is reduced to 142 °C with a capacity of 6.56 wt.%. The E$_a$ of hydrogen desorption in the MgH$_2$-6 wt.% ML-Ti$_3$C$_2$ hydrogen storage system is approximately 99 kJ/mol, which is 35.3% lower than that of pristine MgH$_2$. The enhancement of kinetics in hydrogen absorption and desorption by ML-Ti$_3$C$_2$ can be attributed to two synergistic effects: one is that Ti facilitates the easier dissociation or recombination of hydrogen molecules, while the other is that electron transfer generated by multivalent Ti promotes the easier conversion of hydrogen. These findings help to guide the hydrogen storage properties of metal hydrides doped with MXene.

Keywords: hydrogen storage; magnesium hydride; Ti$_3$C$_2$ MXene; catalyst

1. Introduction

Energy is necessary for the survival and development of human society. In recent years, energy crises and environmental pollution have become increasingly serious with the rapid development of the global economy. The development of new energy is an important means by which to remit the contradiction between economic development and environmental protection. As an ideal secondary energy source, hydrogen energy shows many outstanding advantages, such as a high energy density of 142 MJ/kg [1], a wide range of potential sources, light weight, and environmental friendliness.

Considering that the gaseous-state hydrogen storage system shows lower safety and poor hydrogen storage capacity, metal hydrides possess attractive application prospects. Magnesium hydride (MgH$_2$) shows a high theoretical hydrogen storage capacity of 7.6 wt.%, with the benefits of high capacity, abundant sources, low price, light weight, no pollution, etc. In this regard, MgH$_2$ can be developed with good value as a kind of solid hydrogen storage material [2]. As an ionic compound, the adsorption and desorption process of MgH$_2$ involves the formation and fracture of chemical bonds between hydrogen and metal elements, as well as crystal structure changes. Therefore, the dehydrogenation temperature of MgH$_2$ is higher than 300 °C. In addition, the adsorption and desorption kinetics of MgH$_2$ are poor, resulting in the slow reaction rate of absorption and desorption. The activation energy (E$_a$) of MgH$_2$ is ~143.0–160.6 kJ/mol [3–7]. Therefore, improving the

thermodynamic and kinetic properties of hydrogen absorption/desorption reactions of Mg-based hydrogen storage materials is the key aim of current research.

In order to improve the adsorption and desorption performance of MgH_2 hydrogen storage materials, researchers have modified MgH_2 by alloying [8–12], nanoscaling [13–20], surface modification [21], and catalyst doping [22–28], among others. The addition of a catalyst can significantly reduce the energy barrier of hydrogen absorption and desorption reactions, thus decreasing the reaction temperature and improving the kinetic performance. Among them, Ti-based catalysts [29–33] can effectively improve the hydrogen absorption and desorption characteristics of MgH_2, which has received widespread attention.

MXene is a novel two-dimensional transition metal carbide or carbonitride similar in structure to graphene, which was first synthesized by Gogotsi and Barsoum in 2011 via HF selective etching from its precursor MAX phase [34]. Because of the weak binding force between the A-MX lamellas in the MAX phase, MXene can be eroded from the A atomic layer in the MAX phase with the selection of appropriate etching agents (such as HF, LiF+HCl, NH_4HF_2, etc.) [35]. The general formula of an MXene is expressed as $M_{n+1}X_nT_x$, in which T_x represents the functional groups (–OH, –F, =O, etc.) attached to the surface of the MXene, produced by chemical etching of the precursor MAX phase. At present, dozens of different components of MXenes have been successfully synthesized. As one of the earliest developed MXenes, Ti_3C_2 has attracted wide attention in the fields of lubricants [36,37], environmental pollution control [38], energy storage [39–41], and wave absorption [41,42], among others, due to its unique physical and chemical properties. In recent years, many scholars have used MXenes to improve the hydrogen absorption and desorption performance of hydrogen storage materials, especially Ti_3C_2 MXene. Sheng et al. [43] tried to use $(Ti_{0.5}V_{0.5})_3C_2$ to reduce the initial temperature of the hydrogen desorption of MgH_2 to 210 °C. MgH_2+10 wt.% of $(Ti_{0.5}V_{0.5})_3C_2$ can release hydrogen of 7.0 wt.% at 245 °C, and can absorb 4.8 wt.% of hydrogen at a constant temperature of 120 °C. It was shown that MgH_2 reacted with $(Ti_{0.5}V_{0.5})_3C_2$ to form Ti and V metals, which were suggested to act as active catalysts for the hydrogen sorption process. Gao et al. [44] synthesized a sandwich-like Ti_3C_2/TiO_2 via partial oxidation of Ti_3C_2 MXene. The MgH_2+5 wt.% of Ti_3C_2/TiO_2 can release 5.0 wt.% of hydrogen at a constant temperature of 250 °C, and can absorb 4.0 wt.% of hydrogen at a constant temperature of 125 °C. The layered structures and the Ti-containing compounds with multiple valences were considered to be responsible for the improvement of MgH_2 by Ti_3C_2/TiO_2. Liu et al. [45] synthesized V_2C and Ti_3C_2 MXenes by exfoliating V_2AlC and Ti_3AlC_2. MgH_2+10 wt.% of $2V_2C/Ti_3C_2$ initiated hydrogen desorption at around 180 °C, and 5.1 wt.% of hydrogen was desorbed within 60 min at 225 °C. Hydrogen atoms or molecules may preferentially transfer through the $MgH_2/V_2C/Ti_3C_2$ triple-grain boundaries during the desorption process, and through the Mg/Ti_3C_2 interfaces during the absorption process. V_2C and Ti_3C_2 mainly act as efficient catalysts for MgH_2 at the same time. Gao et al. [46] synthesized a few-layer $Ti_3C_2T_x$ supporting highly dispersed nano-Ni particles through a self-assembly reduction process. MgH_2-5 wt.% $Ni_{30}/FL-Ti_3C_2T_x$ can release approximately 5.83 wt.% hydrogen within 1800 s at 250 °C, and can absorb 5 wt.% hydrogen within 1700 s at 100 °C. This superb hydrogen storage performance was attributed to the combined effects of finely dispersed nano-Ni grown in situ on $FL-Ti_3C_2T_x$, the large specific area of $FL-Ti_3C_2T_x$, multivalent Ti derived from $FL-Ti_3C_2T_x$, and the electronic interaction between Ni and $FL-Ti_3C_2T_x$. Chen et al. [47] introduced Ti_3C_2 into a $4MgH_2-LiAlH_4$ composite; the dehydrogenation onset temperature of the $4MgH_2-LiAlH_4-Ti_3C_2$ composite was decreased by 64 K and 274 K with $4MgH_2-LiAlH_4$ and with as-milled MgH_2, respectively. The destabilization of $4MgH_2-LiAlH_4$ can be ascribed to the Ti formed in situ from the MXene Ti_3C_2. Few-layer Ti_3C_2 can only exist in solution in the form of film, and is easy to agglomerate, which reduces the number of active sites of hydrogen absorption and desorption. In comparison, multilayer Ti_3C_2 ($ML-Ti_3C_2$) can exist in the form of a solid powder, which makes it easier to composite with MgH_2. Therefore, $ML-Ti_3C_2$ may improve the hydrogen absorption and desorption performance of MgH_2.

2. Experimental Details

2.1. Preparation of Material

Multilayer Ti_3C_2 MXene (ML-Ti_3C_2) was prepared by selective etching of Al atoms in Ti_3AlC_2 with an HF/HCl etching agent. The main operation methods were as follows: (1) Preparation of the etching agent: Mixing and stirring 12 mL of HCl (concentration 35–38 wt.%), 2 mL HF (concentration 49 wt.%), and 6 mL deionized water. (2) Etching: 1 g of Ti_3AlC_2 was slowly added to the mixed solution at 35 °C and stirred at 400 rpm for 24 h. (3) Washing: After etching, the suspension was centrifuged at 3500 rpm for 5 min to achieve the precipitation of multilayer MXene. The precipitation was washed with deionized water 5–6 times until the pH of the supernatant was ≥ 6, and then the precipitate was collected. (4) Drying: The collected wet powder was placed in the refrigerator for freezing, then placed in the vacuum freeze-drying oven for 24 h. The water between the layers of MXene was frozen into ice, which led to an increase in the layer spacing. In the vacuum freeze-drying oven, the frozen ice directly sublimated in vacuum to prevent the collapse of the interlayer structure. The lyophilized layers of the MXene were well spaced and accordion-like.

The as-synthesized Ti_3C_2 was introduced into MgH_2 by ball milling. Experimentally, 1 g of MgH_2 (98%, Lanabai Pharmaceutical Chemical Co. Ltd., Wuhan, China) was mixed into the milling jar with the ML-Ti_3C_2 in different proportions (MgH_2+x wt.% ML-Ti_3C_2, x = 4, 6, 8, 10) for ball milling. Argon was used in the milling jar as the protective gas. Ball milling was carried out by all-directional planetary ball mill (PMQ0.4L, Zhuodi Instrument and Equipment Co. Ltd., Shanghai, China) at 400 rpm for 24 h; the ball-to-powder ratio was 30:1. For comparison with the former, 1 g of pristine MgH_2 was ball milled under the same conditions. The whole experimental process was carried out under strict air isolation conditions.

2.2. Characterization Methods

The phase and structure analysis of samples were tested by X-ray diffractometer (XRD, DX-2700B, Hao Yuan Instrument Co., LTD, Dandong, China). The Cu Kα radiation was used for the incident ray (40 kV, 200 mA) in step scan, with a step length of 0.02 °/s and a sampling time of 1 s. Scanning electron microscopy (SEM, Regulus 8230, Hitachi Manufacturing Co. LTD, Tokyo, Japan) and transmission electron microscopy (TEM, JEM-F200, JEOL, Tokyo, Japan) were used to observe the particle size and microstructure of the samples. A microgrid copper mesh was used to hold the samples in the TEM observations. Energy-dispersive spectrometry (EDS, JED-2300T, JEOL, Tokyo, Japan and GENESIS 2000XMS, Hitachi Manufacturing Co. LTD, Tokyo, Japan) coupled with the TEM and SEM was used to analyze the micro-area composition. X-ray photoelectron spectroscopy (XPS, Thermo Scientific K-Alpha+, Thermo Fisher Scientific, Waltham, MA, USA) was utilized to analyze the chemical environments of atoms before and after the experiments. A differential scanning calorimeter (DSC, TGA/DSC2, Mettler-Toledo group, Zurich, Switzerland) was used to study the thermal behavior in hydrogen desorption. The samples were heated from room temperature to 500 °C in an argon atmosphere (20 mL/min) at rates of 5, 7, 9, and 11 °C/min.

2.3. De/Hydrogenation Characterization

The hydrogen absorption and desorption tests were carried out on a Sieverts-type apparatus (Institute of Metal Materials, Zhejiang University, Zhejiang, China). The apparatus was composed of a temperature-controlled tubular furnace, tubular reactors, high-/low-pressure sensors, temperature sensors, connecting pipes, and a test computer. The amount of hydrogen absorption and desorption of the sample was calculated according to the ideal gas state equation. Experimentally, the sample was weighed to ~100 mg in the glove box ($H_2O \leq 0.01$ ppm and $O_2 \leq 0.01$ ppm) each time. During the non-isothermal desorption tests, the sample was heated from room temperature to 400 °C at 2 °C/min at an initial back pressure of 10^{-4} MPa. During the isothermal absorption tests, the initial hydrogen

pressure of 4 MPa was synchronously filled into the reactor, and the sample after hydrogen desorption was heated from room temperature to 300 °C at a heating rate of 2 °C/min. During the isothermal desorption tests, the sample was first heated from room temperature to the target temperature at a rate of 5 °C/min and held for 10 min, and then the valve of the connecting line was quickly opened and kept open for 1 h. During the isothermal absorption tests, the sample was first heated from room temperature to the target temperature at a rate of 5 °C/min and held for 10 min, and then the sample holder was quickly filled with hydrogen at a pressure of 4 MPa and maintained for 1 h. The quantitative information of the experimental details is shown in Table S1.

### 3. Results and Discussion

3.1. Characterization of ML-Ti$_3$C$_2$

ML-Ti$_3$C$_2$ was successfully obtained by selectively etching the Al layers from Ti$_3$AlC$_2$. Figure 1a shows the XRD patterns of as-synthesized Ti$_3$C$_2$ MXene. Through HF etching, the Al lamellas in the precursor MAX were effectively removed. However, the Ti$_3$AlC$_2$ diffraction peak still existed, indicating that the Al lamellas were not completely removed. Thus, the as-synthesized MXene was a mixture of Ti$_3$C$_2$ and Ti$_3$AlC$_2$. In addition, Ti and the F element in HF formed the TiF$_3$ compound. As is shown in Figure 1b, the sample showed an accordion-like multilayer structure of multilayer MXene, with particle sizes ranging from 10 to 15 microns. EDS mapping was performed to observe the element contents, as outlined in Figure S1. EDS mapping shows that the Ti and C elements were distributed uniformly, but residual Al remained in this material, which is consistent with XRD patterns. The higher content of C may be caused by the sample table of the SEM. The presence of O may arise from the oxidation of Ti$_3$C$_2$ or the oxygen-containing functional groups formed after HF etching [48]. Figure 1c displays the TEM image of Ti$_3$C$_2$, in which the lamellar structure of ML-Ti$_3$C$_2$ can be seen. To further observe the microstructure of ML-Ti$_3$C$_2$, high-resolution TEM (HRTEM) was performed, as shown in Figure 1d. The calculated interplanar spacing of 0.265 nm is consistent with the (101) crystal planes of Ti$_3$C$_2$. Therefore, the XRD, SEM, and HRTEM results all confirm the successful synthesis of the ML-Ti$_3$C$_2$ MXene.
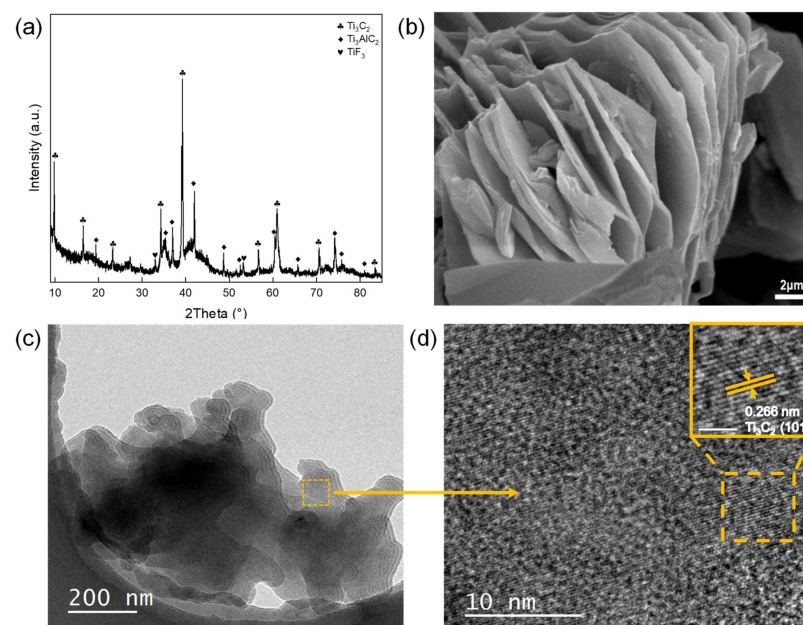
Figure 1. Characterizations of the as-synthesized ML-Ti$_3$C$_2$: (**a**) X-ray diffractometer (XRD) patterns of as-synthesized ML-Ti$_3$C$_2$, (**b**) Scanning electron microscopy (SEM) images, (**c**) transmission electron microscopy (TEM) image, and (**d**) High resolution TEM image.

3.2. De/Hydrogenation Performance of MgH_2+ML-Ti_3C_2

The as-synthesized ML-Ti_3C_2 was introduced into MgH_2 through ball milling to promote the de/hydrogenation performance. The prepared material systems were subjected to non-isothermal hydrogen desorption tests in order to select the best amount of ML-Ti_3C_2 to add. In contrast, as-milled MgH_2 was also tested. Figure 2 displays the non-isothermal hydrogen desorption curves of MgH_2+x wt.% ML-Ti_3C_2, (x = 0, 4, 6, 8, 10). The as-milled MgH_2 begins to release hydrogen at around 267 °C, with a hydrogen desorption capacity of 7.0 wt.%. After the addition of ML-Ti_3C_2, the initial and the peak hydrogen desorption temperatures of the material systems were significantly reduced. With the increase of the amount of ML-Ti_3C_2, the initial dehydrogenation temperature decreases from 182 °C to 137 °C; however, the hydrogen desorption capacity is gradually weakened. The hydrogen desorption temperature and capacity of the material systems are shown in Table S2. When x = 6, the hydrogen desorption temperature reaches 142 °C, which is ~125 °C lower than that of as-milled MgH_2. Continuing to add ML-Ti_3C_2, the initial dehydrogenation temperature decreases inconspicuously. MgH_2-6 wt.% ML-Ti_3C_2 can also fully release its hydrogen when the temperature increases to 227 °C, showing the best overall hydrogen desorption capacity. Therefore, in subsequent experiments, MgH_2-6 wt.% ML-Ti_3C_2 was taken as the object to discuss its hydrogen absorption and desorption performance.
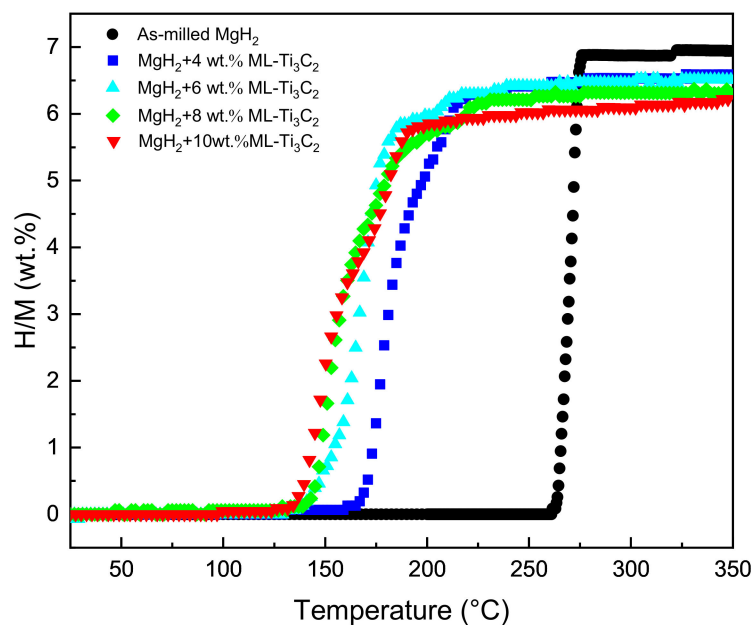
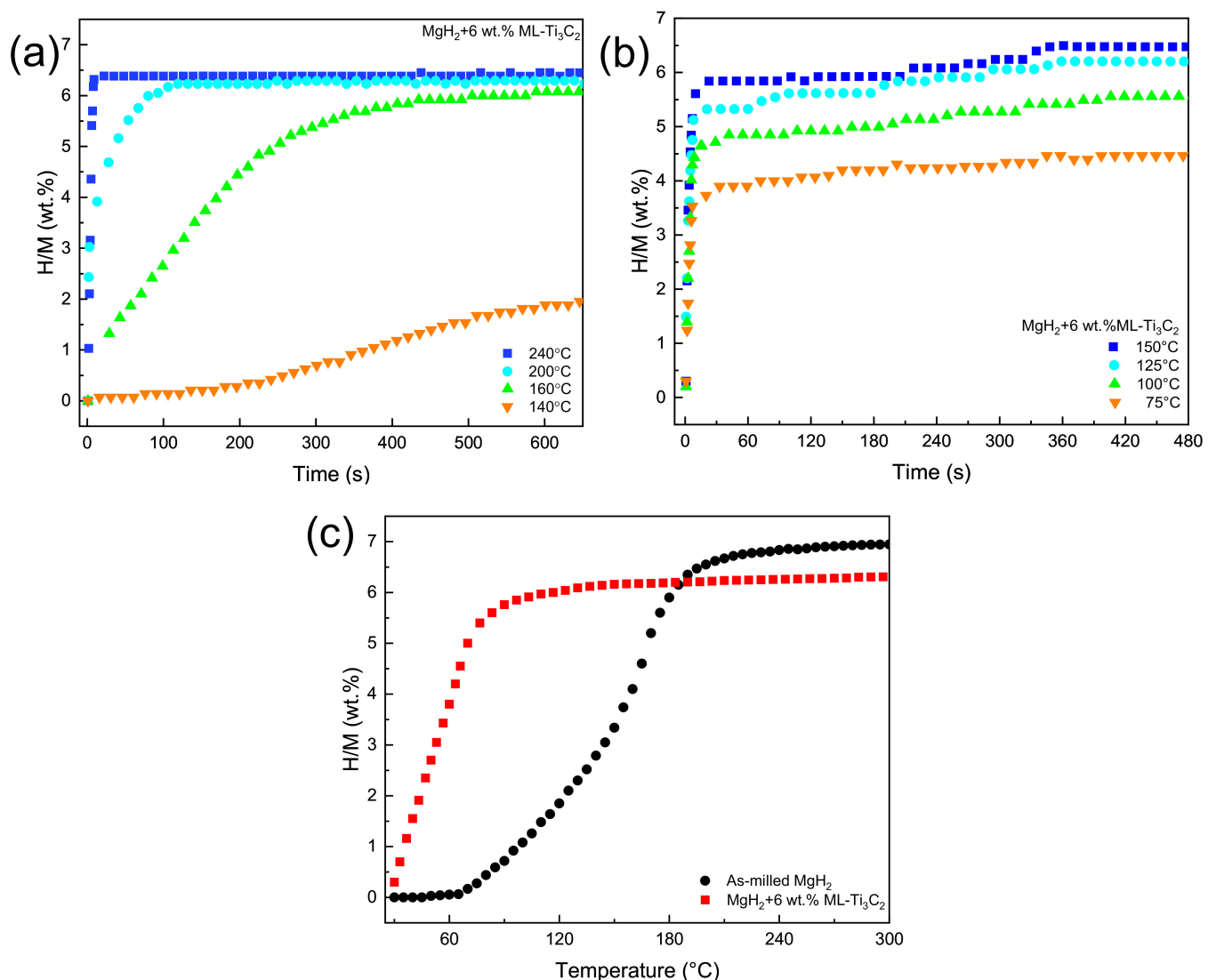**Figure 2.** Hydrogen desorption performances of MgH_2+x wt.% ML-Ti_3C_2 (x = 0, 4, 6, 8, 10).

To further illustrate the optimization of the dehydrogenation kinetics of MgH_2 by Ti_3C_2, isothermal dehydrogenation of MgH_2-6 wt.% ML-Ti_3C_2 was performed at different temperatures. Figure 3a displays dehydrogenation kinetics curves of MgH_2-6 wt.% ML-Ti_3C_2 at 240 °C, 200 °C, 160 °C, and 140 °C. It is apparent that this sample possesses excellent dehydrogenation kinetics performance at 240 °C, with a hydrogen desorption capacity of 6.45 wt.% in only 10 min. In contrast, as-milled MgH_2 does not release hydrogen at same temperature. With the decrease in the test temperature, the initial hydrogen desorption rate of the sample decreases gradually. At 140 °C, there is still 1.95 wt.% of hydrogen that can be released in 10 min, but only 3.63 wt.% can be released in 60 min after extending the test time (Figure S2).

In order to study the effect of ML-Ti_3C_2 on the hydrogen absorption performance of MgH_2, the non-isothermal hydrogen absorption of the MgH_2-6 wt.% ML-Ti_3C_2 system was first tested (with as-milled MgH_2 as a control group). Figure 3c displays the absorption curves of two samples. It should be noted that MgH_2-6 wt.% ML-Ti_3C_2 system shows

excellent hydrogen absorption performance, immediately beginning to absorb hydrogen at room temperature (6.3 wt.%). However, the as-milled MgH_2 after dehydrogenation does not react until 70 °C. The hydrogen absorption temperature of the sample with ML-Ti_3C_2 is reduced by 35 °C. The initial hydrogenation temperature and hydrogen absorption capacity of two samples are outlined in Table S3. Figure 3b displays the isothermal hydrogen absorption curves of the MgH_2-6 wt.% ML-Ti_3C_2 system at temperatures of 150 °C, 125 °C, 100 °C, and 75 °C. All of the curves show excellent hydrogen absorption kinetics, with 150 °C being the best and 75 °C the worst, which reaches more than 80% of the saturated hydrogen absorption capacity of the corresponding temperature within 60 s. In addition, at lower temperatures (75 °C and 100 °C), the hydrogen absorption capacity of the MgH_2-6 wt.% ML-Ti_3C_2 system reaches 4.20 wt.% and 4.86 wt.%, respectively. The initial hydrogenation temperature and de/hydrogenation capacity of MgH_2-6 wt.% ML-Ti_3C_2 are outlined in Table 1. Overall, adding ML-Ti_3C_2 to MgH_2 effectively improves the kinetics of hydrogen adsorption and desorption.

Figure 3. De/hydrogenation performance curves of MgH_2-6 wt.% ML-Ti_3C_2 and as-milled MgH_2. (**a**) Isothermal dehydrogenation curves at different temperatures. (**b**) Isothermal rehydrogenation curves at different temperatures. (**c**) Non-isothermal absorption curves of two samples.

Table 1. The initial hydrogenation temperature and de/hydrogenation capacity of MgH_2-6 wt.% ML-Ti_3C_2.

Hydrogenation Temperature (°C)	Hydrogenation Capacity (wt.%)	Dehydrogenation Temperature (°C)	Dehydrogenation Capacity (wt.%)
150	6.47	240	6.45
125	6.20	200	6.29
100	4.86	160	6.08
75	4.20	140	1.95 (3.63 wt.% in 1 h)

3.3. Kinetics and Thermodynamics of Hydrogen Desorption

DSC analyses were further used to investigate the impact of ML-Ti_3C_2 MXene on the dehydrogenation kinetics thermodynamics of MgH_2. Figure 4a,b show the DSC profiles of MgH_2-6 wt.% ML-Ti_3C_2 and as-milled MgH_2, respectively, at different heating rates (5, 7, 9, and 11 °C/min). With an increase in the heating rate, the hydrogen decomposition peaks shift to higher temperatures. The decomposition of MgH_2-6 wt.% ML-Ti_3C_2 presents two thermal events, which may be caused by uneven grain size [49,50]. Furthermore, the Kissinger equation [51] was utilized to estimate the decomposition energy barrier (E_a) of MgH_2. The Kissinger equation is as follows:

$$\ln (\beta / T_m{}^2) = -E_a / RT_m + A \tag{1}$$

where β represents the heating rate used in the DSC tests, T_m represents the peak temperature in the DSC curves, E_a represents the activation energy, R represents the universal gas constant, and A is also a constant. Figure 4c displays Kissinger's plots and the corresponding fitting lines of MgH_2-6 wt.% ML-Ti_3C_2 and as-milled MgH_2. The fitting equations obtained by the Kissinger equation are as follows:

$$y = (-11.92038 \pm 0.20321)x + (9.11676 \pm 0.33879) \tag{2}$$

$$y = (-18.41333 \pm 0.1712)x + (18.95006 \pm 0.27678) \tag{3}$$

The E_a of dehydrogenation, obtained by the Kissinger equation, is 99.11 ± 1.69kJ/mol and 153.09 ± 1.42 kJ/mol for the composite system and the as-milled MgH_2 respectively. It should be noted that the composite system reduces the activation energy by 35.3%. The addition of ML-Ti_3C_2 makes the hydrogen desorption in the two steps of the system shift to lower temperatures, but the temperature of the first step decreases more greatly. The hydrogen desorption peak in the second step widens noticeably, indicating that Ti_3C_2 improves the first desorption of MgH_2 more greatly [52]. In addition, after the integral of the DSC curve, the enthalpy change of the MgH_2-6 wt.% ML-Ti_3C_2 and the as-milled MgH_2 is approximately 75.46 kJ/mol H_2 and 78.91 kJ/mol H_2, respectively. Therefore, the addition of Ti_3C_2 does not obviously improve the thermodynamic properties. This could be associated with the fact that the introduction of multilayer Ti_3C_2 leads neither to significant particle size refinement of MgH_2 nor to the formation of any kind of solid solution with Ti [53]. The lower dehydrogenation temperature of the composite can effectively contribute to the kinetic improvement of MgH_2 via the addition of ML-Ti_3C_2.
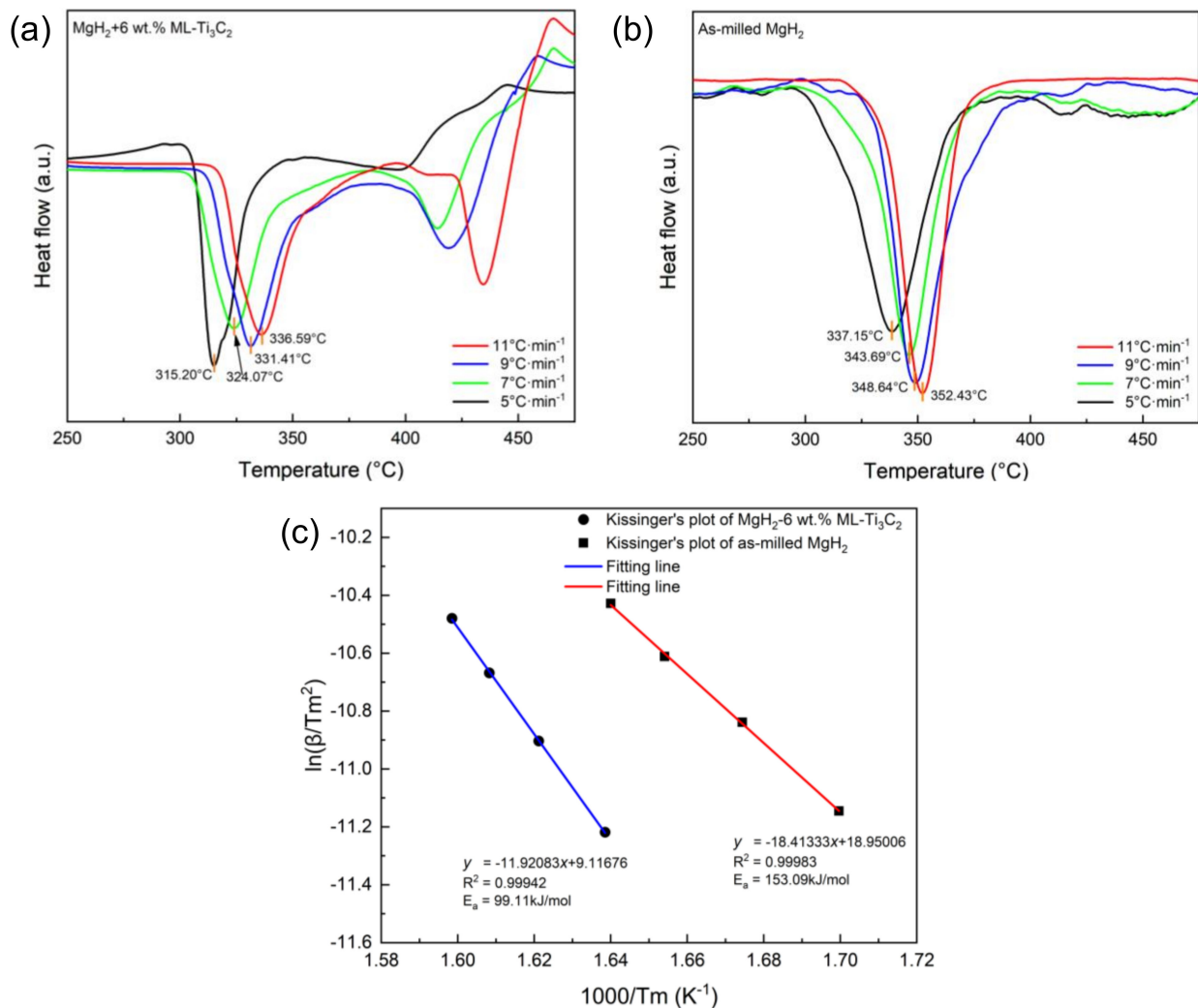
Figure 4. Differential scanning calorimeter (DSC) curves of (**a**) MgH$_2$-6 wt.% ML-Ti$_3$C$_2$ and (**b**) as-milled MgH$_2$ at various heating rates. (**c**) Kissinger's plots and corresponding fitting lines for MgH$_2$-6 wt.% ML-Ti$_3$C$_2$ and as-milled MgH$_2$.

3.4. The Mechanisms for Improving the Hydrogen Storage Properties

To study the mechanisms for improving the hydrogen storage properties of MgH$_2$ via the addition of ML-Ti$_3$C$_2$, the microstructures, morphologies, and valence states of the elements were further analyzed via XRD, SEM, EDS, TEM, and XPS. Figure 5a displays the XRD patterns of as-milled, dehydrogenative, and rehydrogenative MgH$_2$-6 wt.% ML-Ti$_3$C$_2$. After ball milling, the MgH$_2$ phase shows obvious peak broadening and decreased diffraction intensity due to its small particle size and poor crystallinity [54]. In addition, a small amount of MgO and TiO$_2$ is produced, which may be due to the air entering the ball mill tank during ball milling. After dehydrogenation, no MgH$_2$ phase can be observed, indicating that all of that phase has been converted to Mg, but a small amount of MgO impurities still exist. After rehydrogenation, most of the Mg is converted into MgH$_2$, which indicates the good reversibility of the sample in the process of hydrogen absorption and desorption. It is worth noting that no C-related peak value can be detected in the XRD patterns of the three samples, which indicates that the decomposition of ML-Ti$_3$C$_2$ or the lack of strong crystallinity may occur during the balling process, leading to undetectable results.

Figure 5b−e display the SEM images of MgH$_2$-6 wt.% ML-Ti$_3$C$_2$ after (5b) ball milling (5c) dehydrogenation and (5d,e) rehydrogenation. Figure S3a,b display elemental mappings after dehydrogenation and rehydrogenation. The particle sizes of ball-milled and hydrogenated samples range from 0.1 to 2 μm, and the distribution is relatively loose.

As MXene is broken and reduced, Ti and C are uniformly dispersed in the MgH_2 matrix, increasing the number of reactive sites. After rehydrogenation, the particles expand and come into close contact. This close particle contact is not conducive to the hydrogen absorption kinetics of pure MgH_2 [45]. However, with the addition of $ML-Ti_3C_2$, hydrogen can easily be spatially transferred through the interface between MgH_2 and $ML-Ti_3C_2$. In general, the practical catalytic efficiency for solid-phase reactions depends not only on the intrinsic properties of the catalyst, but also on the uniform distribution of the catalytic phases, and their physicochemical interactions with the reacting phases [55]. What can be observed through the electron image and corresponding elemental mappings of MgH_2-6 wt.% $ML-Ti_3C_2$ is that the ball milling of MgH_2 and Ti_3C_2 mixtures results in particle refinement and uniform dispersion of the catalytic phase, which means the Mg, Ti, and C are distributed uniformly in the sample. This uniform distribution provides enough active catalytic sites to significantly improve the hydrogen absorption kinetics of MgH_2.
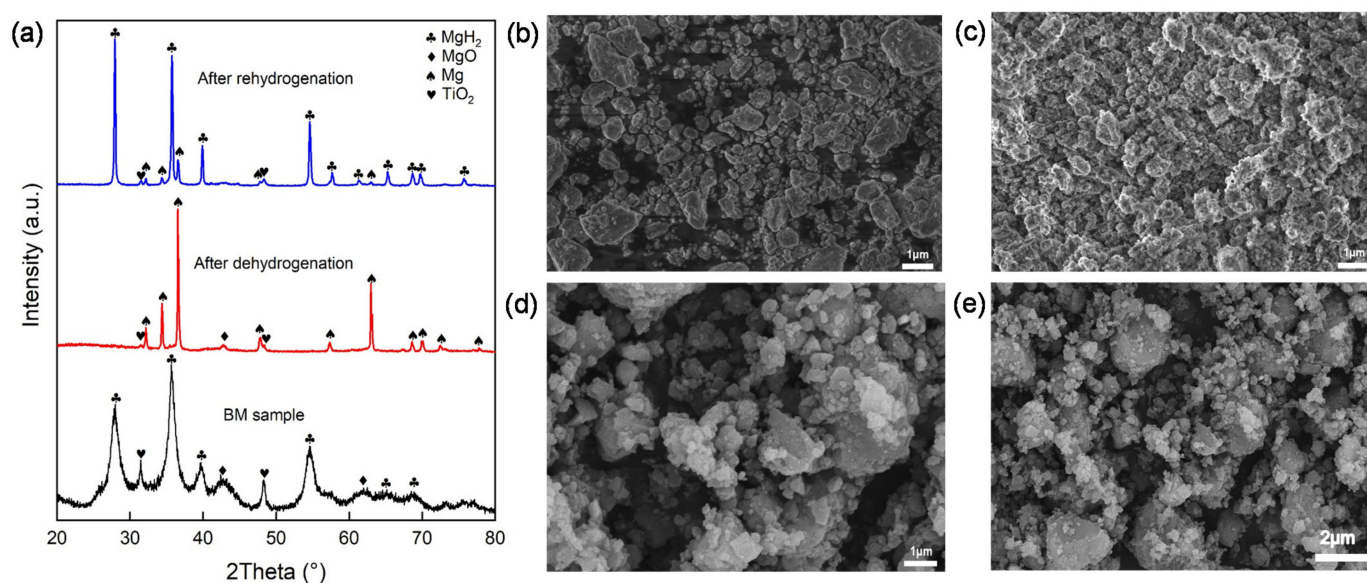
Figure 5. (**a**) XRD patterns of as-milled, dehydrogenative, and rehydrogenative MgH_2-6 wt.% $ML-Ti_3C_2$. (**b**) SEM image of MgH_2-6 wt.% $ML-Ti_3C_2$ after ball milling. (**c**) SEM image of MgH_2-6 wt.% $ML-Ti_3C_2$ after dehydrogenation. (**d**,**e**) SEM images of MgH_2-6 wt.% $ML-Ti_3C_2$ after rehydrogenation.

Figure 6a,b display the XPS spectra of C 1s and Ti 2p of the as-milled, dehydrogenative, and rehydrogenative MgH_2-6 wt.% $ML-Ti_3C_2$. The C 1s XPS spectrum can be divided into four peaks: 282.0 eV, 284.8 eV, 286.5 eV, and 288.9 eV, which can be fitted to Ti−C [43], C−C [56], C−O [57], and O=C−O [57], respectively. It can be observed that Ti−C exists, hardly changes, and cannot be completely broken through ball milling, dehydrogenation, or rehydrogenation. The Ti 2p XPS spectrum after ball milling is parallel to four sets of $2p_{1/2}−2p_{3/2}$ spin−orbit doublets at 453.7/459.8 eV, 455.1/460.9 eV, 457.0/462.2 eV, and 458.9/464.6 eV, which can be fitted to Ti^0 [52], Ti−C [43], Ti^{3+} [58], and TiO_2 [59], respectively. The appearance of Ti^0 and Ti^{3+} indicates a possible chemical reduction reaction between $ML-Ti_3C_2$ and MgH_2, which reduces Ti_3C_2 to Ti^0 and Ti^{3+} during ball milling. After dehydrogenation, Ti^{2+} (456.4/461.5 eV) [57] appears, except for Ti^0, Ti−C, Ti^{3+}, and TiO_2, indicating that the Ti^{3+} is further reduced to form Ti^{2+}. After rehydrogenation, the content of Ti^{2+} increases, indicating that the reduction reaction of Ti is accompanied by the hydrogen absorption and desorption reaction.
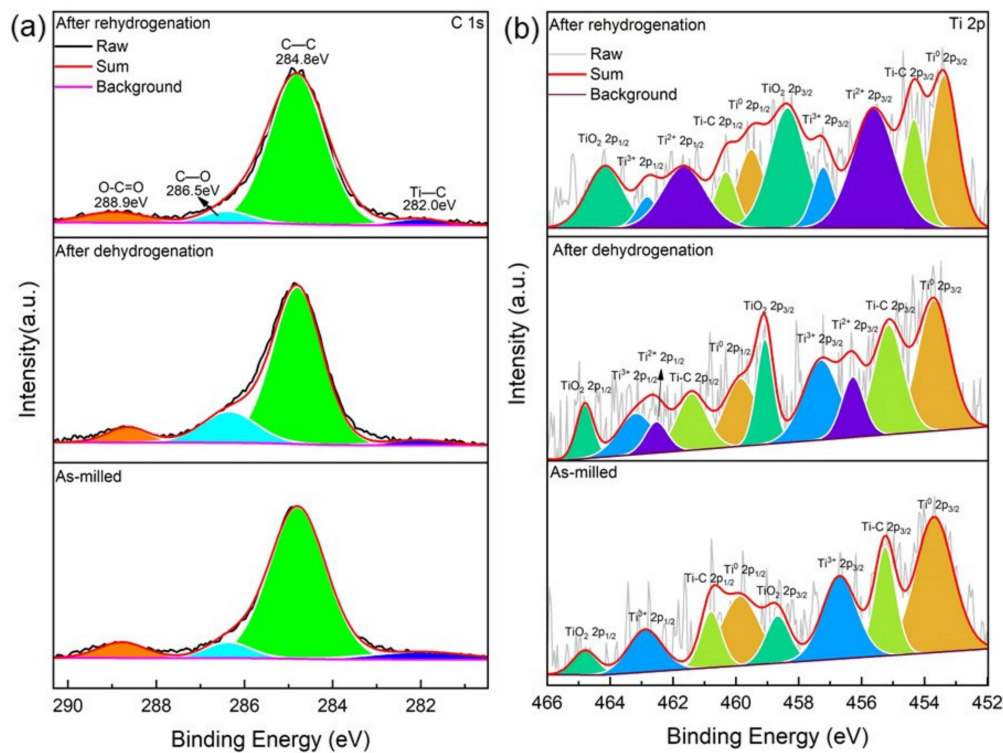
Figure 6. X-ray photoelectron spectroscopy (XPS) spectra of C 1s (**a**) and Ti 2p (**b**) of the as-milled, dehydrogenative, and rehydrogenative MgH_2-6 wt.% ML-Ti_3C_2.

To further prove the points detailed above, Figure 7a,b show the EDS mappings of MgH_2-6 wt.% ML-Ti_3C_2 after ball milling, and TEM and HRTEM images of the as-milled MgH_2-6 wt.% ML-Ti_3C_2. Layered structures cannot be found via the TEM image. Combined with the EDS mappings, the microstructures of ML-Ti_3C_2 collapse, and are well dispersed on the MgH_2 particles. The HRTEM analysis in Figure 7b clearly shows the different kinds of interplanar spacings (0.190, 0.221, 0.199, 0.210, 0.214, 0.153, and 0.235 nm), corresponding to the crystal planes of Mg(102), MgH_2(200), MgH_2(210), MgO(200),Ti(002), Ti_3C_2(105), TiO_2(213), and Ti(002), respectively. Taking the TEM images, XRD patterns, and XPS spectra into account, it appears that a series of redox reactions occurred during the ball milling. A part of Ti−C fractured, Ti^{3+} and Ti^{2+} were reduced to form metallic Ti, $H^−$ was oxidized into H_2, and Mg^{2+} was reduced to form metallic Mg. In addition, on account of a small amount of O_2 having seeped into the ball mill tank, Mg and Ti combined with O_2 to form MgO and TiO_2, respectively. Some reaction equations during the ball milling are as follows:

$$Ti^{3+} + 3e^− = Ti \tag{4}$$

$$Ti^{2+} + 2e^− = Ti \tag{5}$$

$$2H^− − 2e^− = H_2 \uparrow \tag{6}$$

$$Mg^{2+} + 2e^− = Mg \tag{7}$$

Based on the characterization analysis results above, the mechanisms by which ML-Ti_3C_2 improves the kinetic performance of hydrogen absorption and desorption by MgH_2 can be preliminarily described. In the ball milling process, the zero-valent titanium formed in situ is uniformly dispersed on the surface of MgH_2, which increases the active site of hydrogen absorption and desorption. In addition, Ti can make the hydrogen molecules on its surface easier to dissociate and recombine [60]. At the interface of MgH_2-6 wt.% ML-Ti_3C_2, the displacement of Ti and Mg formed in situ in the MgH_2 results in the deformation of MgH_2 structure, which can destroy the Mg–H bond and generate

vacancies [61]. The electron transfer caused by the change in Ti valence in the process of dehydrogenation and rehydrogenation can promote the recombination of hydrogen atoms into hydrogen molecules [33], as well as the conversion between Mg^{2+} and Mg, or between H^- and H_2 [62], thus promoting the hydrogen absorption/desorption kinetics of MgH_2. In conclusion, the enhancement of hydrogen absorption and desorption kinetics by ML-Ti_3C_2 can be attributed to two synergistic effects: one is that Ti facilitates the easier dissociation or recombination of hydrogen molecules, while the other is that the electron transfer generated by multivalent Ti promotes the easier conversion of hydrogen.
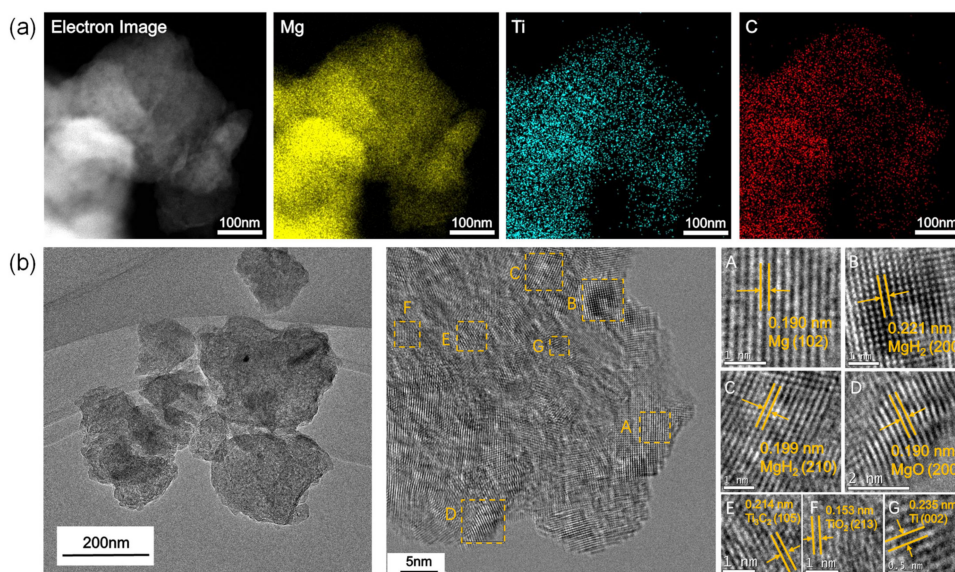
Figure 7. (**a**) Electron image and corresponding elemental mappings of MgH_2-6 wt.% ML-Ti_3C_2 after ball milling, and (**b**) TEM and HRTEM images of the as-milled MgH_2-6 wt.% ML-Ti_3C_2 (A–G: Subfigures of the middle image of Figure 2. (**b**) and corresponding interplanar spacings).

4. Conclusions

Multilayer Ti_3C_2 MXene was prepared by etching the precursor Ti_3AlC_2, and was then introduced into MgH_2 by ball milling. The best performance of MgH_2-x wt.% ML-Ti_3C_2 composite hydrogen storage materials prepared with different addition ratios reached an initial desorption temperature of 142 °C with a desorption amount of 6.56 wt.%, which is 125 °C lower than the initial desorption temperature of pristine MgH_2. Outstanding hydrogen absorption and desorption performance indicates that the two-dimensional structure similar to that of graphene generates a large number of active sites and a high specific surface area, effectively facilitating the transport and diffusion of hydrogen in the system. The activation energy decreases from approximately 153 kJ/mol of pristine MgH_2 to approximately 99 kJ/mol of MgH_2-6 wt.% ML-Ti_3C_2—a decrease of 35.3%. DSC shows that the addition of ML-Ti_3C_2 does not significantly improve the thermodynamic properties, but greatly improves the kinetic properties of desorption. After dehydrogenation, hydrogen absorption easily begins at room temperature, which is 40 °C lower than that of pristine MgH_2, while the amount of hydrogen absorption reaches 6.3 wt.%, showing good reversibility. In the ball milling process, the metallic Ti formed in situ is uniformly dispersed on the surface of MgH_2, which increases the number of active sites of hydrogen absorption and desorption, and simultaneously promotes the dissociation of hydrogen molecules. The conversion between Mg^{2+}/Mg and H^-/H is promoted by electron transfer due to the change in Ti valence during dehydrogenation and rehydrogenation. The enhancement of hydrogen absorption and desorption kinetics by Ti_3C_2 can be attributed to the joint result of Ti facilitating the easier dissociation or recombination of hydrogen

molecules, along with the electron transfer generated by multivalent Ti facilitating the easier conversion of hydrogen.

References

1. Schapbach, L.; Zuttel, A. Hydrogen-storage materials for mobile applications. *Nature* **2001**, *414*, 353–358. [CrossRef]
2. Jia, Y.; Sun, C.; Shen, S.; Zou, J.; Mao, S.S.; Yao, X. Combination of nanosizing and interfacial effect: Future perspective for designing Mg-based nanomaterials for hydrogen storage. *Renew. Sustain. Energy Rev.* **2015**, *44*, 289–303. [CrossRef]
3. Chen, G.; Zhang, Y.; Chen, J.; Guo, X.; Zhu, Y.; Li, L. Enhancing hydrogen storage performances of MgH2 by Ni nano-particles over mesoporous carbon CMK-3. *Nanotechnology* **2018**, *29*, 265705. [CrossRef]
4. Fan, M.-Q.; Liu, S.-S.; Zhang, Y.; Zhang, J.; Sun, L.-X.; Xu, F. Superior hydrogen storage properties of MgH2-10 wt.% TiC composite. *Energy* **2010**, *35*, 3417–3421. [CrossRef]
5. Ma, T.; Isobe, S.; Wang, Y.; Hashimoto, N.; Ohnuki, S. Catalytic Effect of Nb2O5 in MgH2-Nb2O5 Ball-Milled Composites. *Catalysts* **2012**, *2*, 344–351. [CrossRef]
6. Malka, I.E.; Czujko, T.; Bystrzycki, J. Catalytic effect of halide additives ball milled with magnesium hydride. *Int. J. Hydrogen Energy* **2010**, *35*, 1706–1712. [CrossRef]
7. Mao, J.; Guo, Z.; Yu, X.; Liu, H.; Wu, Z.; Ni, J. Enhanced hydrogen sorption properties of Ni and Co-catalyzed MgH2. *Int. J. Hydrogen Energy* **2010**, *35*, 4569–4575. [CrossRef]
8. De Lima Andreani, G.F.; Martins Triques, M.R.; Kiminami, C.S.; Botta, W.J.; Roche, V.; Jorge, A.M., Jr. Characterization of hydrogen storage properties of Mg-Fe-CNT composites prepared by ball milling, hot-extrusion and severe plastic deformation. *Int. J. Hydrogen Energy* **2016**, *41*, 23092–23098. [CrossRef]
9. Gkanas, E.I.; Damian, A.; Ioannidou, A.; Stoian, G.; Lupu, N.; Gjoka, M.; Makridis, S.S. Synthesis, characterisation and hydrogen sorption properties of mechanically alloyed Mg(Ni1-xMnx)(2). *Mater. Today Energy* **2019**, *13*, 186–194. [CrossRef]
10. Luo, Q.; Li, J.; Li, B.; Liu, B.; Shao, H.; Li, Q. Kinetics in Mg-based hydrogen storage materials: Enhancement and mechanism. *J. Magnes. Alloy.* **2019**, *7*, 58–71. [CrossRef]
11. Skryabina, N.; Aptukov, V.; Romanov, P.; Fruchart, D.; de Rango, P.; Girard, G.; Grandini, C.; Sandim, H.; Huot, J.; Lang, J.; et al. Microstructure Optimization of Mg-Alloys by the ECAP Process Including Numerical Simulation, SPD Treatments, Characterization, and Hydrogen Sorption Properties. *Molecules* **2019**, *24*, 89. [CrossRef]
12. Yong, H.; Guo, S.; Yuan, Z.; Qi, Y.; Zhao, D.; Zhang, Y. Phase transformation, thermodynamics and kinetics property of Mg90Ce5RE5 (RE = La, Ce, Nd) hydrogen storage alloys. *J. Mater. Sci. Technol.* **2020**, *51*, 84–93. [CrossRef]
13. Liu, Y.; Zou, J.; Zeng, X.; Wu, X.; Tian, H.; Ding, W.; Wang, J.; Walter, A. Study on hydrogen storage properties of Mg nanoparticles confined in carbon aerogels. *Int. J. Hydrogen Energy* **2013**, *38*, 5302–5308. [CrossRef]
14. Schneemann, A.; White, J.L.; Kang, S.; Jeong, S.; Wan, L.F.; Cho, E.S.; Heo, T.W.; Prendergast, D.; Urban, J.J.; Wood, B.C.; et al. Nanostructured Metal Hydrides for Hydrogen Storage. *Chem. Rev.* **2018**, *118*, 10775–10839. [CrossRef] [PubMed]
15. Sun, Y.; Ma, T.; Aguey-Zinsou, K.-F. Magnesium Supported on Nickel Nanobelts for Hydrogen Storage: Coupling Nanosizing and Catalysis. *Acs. Appl. Nano Mater.* **2018**, *1*, 1272–1279. [CrossRef]
16. Vajo, J.; Pinkerton, F.; Stetson, N. Nanoscale phenomena in hydrogen storage. *Nanotechnology* **2009**, *20*, 200201. [CrossRef] [PubMed]
17. Xia, G.; Tan, Y.; Chen, X.; Sun, D.; Guo, Z.; Liu, H.; Ouyang, L.; Zhu, M.; Yu, X. Monodisperse Magnesium Hydride Nanoparticles Uniformly Self-Assembled on Graphene. *Adv. Mater.* **2015**, *27*, 5981–5988. [CrossRef]

18. Xia, G.; Tan, Y.; Wu, F.; Fang, F.; Sun, D.; Guo, Z.; Huang, Z.; Yu, X. Graphene-wrapped reversible reaction for advanced hydrogen storage. *Nano Energy* **2016**, *26*, 488–495. [CrossRef]

19. Yu, X.; Tang, Z.; Sun, D.; Ouyang, L.; Zhu, M. Recent advances and remaining challenges of nanostructured materials for hydrogen storage applications. *Prog. Mater. Sci.* **2017**, *88*, 1–48. [CrossRef]

20. Zhang, Q.; Huang, Y.; Xu, L.; Zang, L.; Guo, H.; Jiao, L.; Yuan, H.; Wang, Y. Highly Dispersed MgH2 Nanoparticle-Graphene Nanosheet Composites for Hydrogen Storage. *Acs. Appl. Nano Mater.* **2019**, *2*, 3828–3835. [CrossRef]

21. Aktekin, B.; Eyovge, C.; Ozturk, T. Carbon coating of magnesium particles. *J. Alloy. Compd.* **2017**, *720*, 17–21. [CrossRef]

22. Huang, Y.; An, C.; Zhang, Q.; Zang, L.; Shao, H.; Liu, Y.; Zhang, Y.; Yuan, H.; Wang, C.; Wang, Y. Cost-effective mechanochemical synthesis of highly dispersed supported transition metal catalysts for hydrogen storage. *Nano Energy* **2021**, *80*, 105535. [CrossRef]

23. Liu, J.; Ma, Z.; Liu, Z.; Tang, Q.; Zhu, Y.; Lin, H.; Zhang, Y.; Zhang, J.; Liu, Y.; Li, L. Synergistic effect of rGO supported Ni3Fe on hydrogen storage performance of MgH2. *Int. J. Hydrogen Energy* **2020**, *45*, 16622–16633. [CrossRef]

24. Ma, Z.; Zhang, J.; Zhu, Y.; Lin, H.; Liu, Y.; Zhang, Y.; Zhu, D.; Li, L. Facile Synthesis of Carbon Supported Nano-Ni Particles with Superior Catalytic Effect on Hydrogen Storage Kinetics of MgH2. *Acs. Appl. Energy Mater.* **2018**, *1*, 1158–1165. [CrossRef]

25. Meena, P.; Singh, R.; Sharma, V.K.; Jain, I.P. Role of NiMn9.3Al4.0Co14.1Fe3.6 alloy on dehydrogenation kinetics of MgH2. *J. Magnes. Alloy.* **2018**, *6*, 318–325. [CrossRef]

26. Sulaiman, N.N.; Juahir, N.; Mustafa, S.; Yap, F.A.H.; Ismail, M. Improved hydrogen storage properties of MgH2 catalyzed with K2NiF6. *J. Energy Chem.* **2016**, *25*, 832–839. [CrossRef]

27. Yahya, M.S.; Ismail, M. Catalytic effect of SrTiO3 on the hydrogen storage behaviour of MgH2. *J. Energy Chem.* **2019**, *28*, 46–53. [CrossRef]

28. Yao, P.; Jiang, Y.; Liu, Y.; Wu, C.; Chou, K.-C.; Lyu, T.; Li, Q. Catalytic effect of Ni@rGO on the hydrogen storage properties of MgH2. *J. Magnes. Alloy.* **2020**, *8*, 461–471. [CrossRef]

29. Grzech, A.; Lafont, U.; Magusin, P.C.M.M.; Mulder, F.M. Microscopic Study of TiF3 as Hydrogen Storage Catalyst for MgH2. *J. Phys. Chem. C* **2012**, *116*, 26027–26035. [CrossRef]

30. Shao, H.; Felderhoff, M.; Schueth, F.; Weidenthaler, C. Nanostructured Ti-catalyzed MgH2 for hydrogen storage. *Nanotechnology* **2011**, *22*, 235401. [CrossRef] [PubMed]

31. Wang, J.S.; Zhang, W.; Han, S.M.; Qin, F. Improvement in hydrogen storage properties of MgH$_2$ catalyzed with BaTiO$_3$ additive. In Proceedings of the 2nd International Conference on New Material and Chemical Industry, Sanya, China, 13–15 November 2021.

32. Zhang, L.; Chen, L.; Fan, X.; Xiao, X.; Zheng, J.; Huang, X. Enhanced hydrogen storage properties of MgH$_2$ with numerous hydrogen diffusion channels provided by Na$_2$Ti$_3$O$_7$ nanotubes. *J. Mater. Chem. A* **2017**, *5*, 6178–6185. [CrossRef]

33. Cui, J.; Wang, H.; Liu, J.; Ouyang, L.; Zhang, Q.; Sun, D.; Yao, X.; Zhu, M. Remarkable enhancement in dehydrogenation of MgH2 by a nano-coating of multi-valence Ti-based catalysts. *J. Mater. Chem. A* **2013**, *1*, 5603–5611. [CrossRef]

34. Naguib, M.; Mochalin, V.N.; Barsoum, M.W.; Gogotsi, Y.G. Two-Dimensional Materials: 25th Anniversary Article: MXenes: A New Family of Two-Dimensional Materials (Adv. Mater. 7/2014). *Adv. Mater.* **2014**, *26*, 982. [CrossRef]

35. Hu, Q.; Sun, D.; Wu, Q.; Wang, H.; Wang, L.; Liu, B.; Zhou, A.; He, J. MXene: A New Family of Promising Hydrogen Storage Medium. *J. Phys. Chem. A* **2013**, *117*, 14253–14260. [CrossRef] [PubMed]

36. Zhang, X.; Xue, M.; Yang, X.; Wang, Z.; Luo, G.; Huang, Z.; Sui, X.; Li, C. Preparation and tribological properties of Ti3C2(OH)(2) nanosheets as additives in base oil. *Rsc Adv.* **2015**, *5*, 2762–2767. [CrossRef]

37. Zhang, H.; Wang, L.; Chen, Q.; Li, P.; Zhou, A.; Cao, X.; Hu, Q. Preparation, mechanical and anti-friction performance of MXene/polymer composites. *Mater. Des.* **2016**, *92*, 682–689. [CrossRef]

38. Zhang, X.; Lei, J.; Wu, D.; Zhao, X.; Jing, Y.; Zhou, Z. A Ti-anchored Ti2CO2 monolayer (MXene) as a single-atom catalyst for CO oxidation. *J. Mater. Chem. A* **2016**, *4*, 4871–4876. [CrossRef]

39. Xie, Y.; Naguib, M.; Mochalin, V.N.; Barsoum, M.W.; Gogotsi, Y.; Yu, X.; Nam, K.-W.; Yang, X.-Q.; Kolesnikov, A.I.; Kent, P.R.C. Role of Surface Structure on Li-Ion Energy Storage Capacity of Two-Dimensional Transition-Metal Carbides. *J. Am. Chem. Soc.* **2014**, *136*, 6385–6394. [CrossRef]

40. Yan, P.; Zhang, R.; Jia, J.; Wu, C.; Zhou, A.; Xu, J.; Zhang, X. Enhanced supercapacitive performance of delaminated two-dimensional titanium carbide/carbon nanotube composites in alkaline electrolyte. *J. Power Sources* **2015**, *284*, 38–43. [CrossRef]

41. Yun, T.; Kim, H.; Iqbal, A.; Cho, Y.S.; Lee, G.S.; Kim, M.-K.; Kim, S.J.; Kim, D.; Gogotsi, Y.; Kim, S.O.; et al. Electromagnetic Shielding of Monolayer MXene Assemblies. *Adv. Mater.* **2020**, *32*, e1906769. [CrossRef] [PubMed]

42. Liu, J.; Zhang, H.-B.; Sun, R.; Liu, Y.; Liu, Z.; Zhou, A.; Yu, Z.-Z. Hydrophobic, Flexible, and Lightweight MXene Foams for High-Performance Electromagnetic-Interference Shielding. *Adv. Mater.* **2017**, *29*, 1702367. [CrossRef]

43. Shen, Z.; Wang, Z.; Zhang, M.; Gao, M.; Hu, J.; Du, F.; Liu, Y.; Pan, H. A novel solid-solution MXene (Ti0.5V0.5)3C2 with high catalytic activity for hydrogen storage in MgH$_2$. *Materialia* **2018**, *1*, 114–120. [CrossRef]

44. Gao, H.; Liu, Y.; Zhu, Y.; Zhang, J.; Li, L. Catalytic effect of sandwich-like Ti3C2/TiO2(A)-C on hydrogen storage performance of MgH2. *Nanotechnology* **2020**, *31*, 115404. [CrossRef]

45. Liu, H.Z.; Lu, C.L.; Wang, X.C.; Xu, L.; Huang, X.T.; Wang, X.H.; Ning, H.; Lan, Z.Q.; Guo, J. Combinations of V$_2$C and Ti$_3$C$_2$ MXenes for Boosting the Hydrogen Storage Performances of MgH$_2$. *Acs Appl. Mater. Interfaces* **2021**, *13*, 13235–13247. [CrossRef] [PubMed]

46. Gao, H.; Shao, Y.; Shi, R.; Liu, Y.; Zhu, J.; Liu, J.; Zhu, Y.; Zhang, J.; Li, L.; Hu, X. Effect of Few-Layer Ti$_3$C$_2$Tx Supported Nano-Ni via Self-Assembly Reduction on Hydrogen Storage Performance of MgH$_2$. *Acs. Appl. Mater. Interfaces* **2020**, *12*, 47684–47694. [CrossRef]

47. Chen, G.; Zhang, Y.; Cheng, H.; Zhu, Y.; Li, L.; Lin, H. Effects of two-dimension MXene Ti3C2 on hydrogen storage performances of MgH2-LiAlH4 composite. *Chem. Phys.* **2019**, *522*, 178–187. [CrossRef]

48. Wang, Z.; Yu, K.; Feng, Y.; Qi, R.; Ren, J.; Zhu, Z. VO2(p)-V2C(MXene) Grid Structure as a Lithium Polysulfide Catalytic Host for High-Performance Li–S Battery. *ACS Appl. Mater. Interfaces* **2019**, *11*, 44282–44292. [CrossRef] [PubMed]

49. Shang, C.X.; Guo, Z.X. Effect of carbon on hydrogen desorption and absorption of mechanically milled MgH 2. *J. Power Sources* **2004**, *129*, 73–80. [CrossRef]

50. Wang, Y.; Li, L.; An, C.; Wang, Y.; Chen, C.; Jiao, L.; Yuan, H. Facile synthesis of TiN decorated graphene and its enhanced catalytic effects on dehydrogenation performance of magnesium hydride. *Nanoscale* **2014**, *6*, 6684. [CrossRef]

51. Blaine, R.L.; Kissinger, H.E. Homer Kissinger and the Kissinger equation. *Thermochim. Acta* **2012**, *540*, 1–6. [CrossRef]

52. Liu, Y.F.; Du, H.F.; Zhang, X.; Yang, Y.X.; Gao, M.X.; Pan, H.G. Superior catalytic activity derived from a two-dimensional Ti3C2 precursor towards the hydrogen storage reaction of magnesium hydride. *Chem. Commun.* **2016**, *52*, 705–708. [CrossRef]

53. Zhu, W.; Panda, S.; Lu, C.; Ma, Z.; Khan, D.; Dong, J.; Sun, F.; Xu, H.; Zhang, Q.; Zou, J. Using a Self-Assembled Two-Dimensional MXene-Based Catalyst (2D-Ni@Ti3C2) to Enhance Hydrogen Storage Properties of MgH2. *Acs. Appl. Mater. Interfaces* **2020**, *12*, 50333–50343. [CrossRef] [PubMed]

54. Wang, Z.Y.; Zhang, X.L.; Ren, Z.H.; Liu, Y.; Hu, J.J.; Li, H.W.; Gao, M.X.; Pan, H.G.; Liu, Y.F. In situ formed ultrafine NbTi nanocrystals from a NbTiC solid-solution MXene for hydrogen storage in MgH2. *J. Mater. Chem. A* **2019**, *7*, 14244–14252. [CrossRef]

55. Huang, X.; Xiao, X.; Zhang, W.; Fan, X.; Zhang, L.; Cheng, C.; Li, S.; Ge, H.; Wang, Q.; Chen, L. Transition metal (Co, Ni) nanoparticles wrapped with carbon and their superior catalytic activities for the reversible hydrogen storage of magnesium hydride. *Phys. Chem. Chem. Phys.* **2017**, *19*, 4019–4029. [CrossRef] [PubMed]

56. Narayanasamy, M.; Kirubasankar, B.; Shi, M.; Velayutham, S.; Wang, B.; Angaiah, S.; Yan, C. Morphology restrained growth of V(2)O(5)by the oxidation of V-MXenes as a fast diffusion controlled cathode material for aqueous zinc ion batteries. *Chem. Commun.* **2020**, *56*, 6412–6415. [CrossRef]

57. Halim, J.; Cook, K.M.; Naguib, M.; Eklund, P.; Gogotsi, Y.; Rosen, J.; Barsoum, M.W. X-ray photoelectron spectroscopy of select multi-layered transition metal carbides (MXenes). *Appl. Surf. Sci.* **2016**, *362*, 406–417. [CrossRef]

58. Xian, K.; Gao, M.; Li, Z.; Gu, J.; Shen, Y.; Wang, S.; Yao, Z.; Liu, Y.; Pan, H. Superior Kinetic and Cyclic Performance of a 2D Titanium Carbide Incorporated 2LiH+MgB2 Composite toward Highly Reversible Hydrogen Storage. *Acs. Appl. Energy Mater.* **2019**, *2*, 4853–4864. [CrossRef]

59. Zhang, X.; Leng, Z.; Gao, M.; Hu, J.; Du, F.; Yao, J.; Pan, H.; Liu, Y. Enhanced hydrogen storage properties of MgH2 catalyzed with carbon-supported nanocrystalline TiO2. *J. Power Sources* **2018**, *398*, 183–192. [CrossRef]

60. Tan, Y.; Zhu, Y.; Li, L. Excellent catalytic effects of multi-walled carbon nanotube supported titania on hydrogen storage of a Mg-Ni alloy. *Chem. Commun.* **2015**, *51*, 2368–2371. [CrossRef] [PubMed]

61. Cui, J.; Liu, J.; Wang, H.; Ouyang, L.; Sun, D.; Zhu, M.; Yao, X. Mg-TM (TM: Ti, Nb, V, Co, Mo or Ni) core-shell like nanostructures: Synthesis, hydrogen storage performance and catalytic mechanism. *J. Mater. Chem. A* **2014**, *2*, 9645–9655. [CrossRef]

62. Chen, M.; Xiao, X.; Zhang, M.; Liu, M.; Huang, X.; Zheng, J.; Zhang, Y.; Jiang, L.; Chen, L. Excellent synergistic catalytic mechanism of in-situ formed nanosized Mg2Ni and multiple valence titanium for improved hydrogen desorption properties of magnesium hydride. *Int. J. Hydrogen Energy* **2019**, *44*, 1750–1759. [CrossRef]